



HAL
open science

Nightside Auroral Electrons at Mars: Upstream Drivers and Ionospheric Impact

Shaosui Xu, David L. Mitchell, James P. Mcfadden, Christopher M. Fowler, Kathleen Hanley, Tristan Weber, David A. Brain, Gina A. Dibraccio, Michael W. Liemohn, Robert J. Lillis, et al.

► **To cite this version:**

Shaosui Xu, David L. Mitchell, James P. Mcfadden, Christopher M. Fowler, Kathleen Hanley, et al.. Nightside Auroral Electrons at Mars: Upstream Drivers and Ionospheric Impact. Journal of Geophysical Research Space Physics, 2022, 127, 10.1029/2022JA030801 . insu-03867449

HAL Id: insu-03867449

<https://insu.hal.science/insu-03867449>

Submitted on 7 Apr 2023

HAL is a multi-disciplinary open access archive for the deposit and dissemination of scientific research documents, whether they are published or not. The documents may come from teaching and research institutions in France or abroad, or from public or private research centers.

L'archive ouverte pluridisciplinaire **HAL**, est destinée au dépôt et à la diffusion de documents scientifiques de niveau recherche, publiés ou non, émanant des établissements d'enseignement et de recherche français ou étrangers, des laboratoires publics ou privés.

Copyright

JGR Space Physics

RESEARCH ARTICLE

10.1029/2022JA030801

Key Points:

- The occurrence rates of auroral electrons increase but their integrated energy fluxes somewhat decrease with increasing upstream drivers
- We quantify the planetary ion density enhancement resulting from auroral electron precipitation to be up to an order of magnitude
- Auroral electron precipitation occurs more frequently and is more intense over strong crustal fields than weak crustal fields

Correspondence to:

S. Xu,
shaosui.xu@ssl.berkeley.edu

Citation:

Xu, S., Mitchell, D. L., McFadden, J. P., Fowler, C. M., Hanley, K., Weber, T., et al. (2022). Nightside auroral electrons at Mars: Upstream drivers and ionospheric impact. *Journal of Geophysical Research: Space Physics*, 127, e2022JA030801. <https://doi.org/10.1029/2022JA030801>

Received 30 JUN 2022
 Accepted 20 AUG 2022

Nightside Auroral Electrons at Mars: Upstream Drivers and Ionospheric Impact

Shaosui Xu¹ , David L. Mitchell¹ , James P. McFadden¹, Christopher M. Fowler² , Kathleen Hanley¹ , Tristan Weber³, David A. Brain⁴ , Gina A. DiBraccio³ , Michael W. Liemohn⁵ , Robert J. Lillis¹ , Jasper S. Halekas⁶ , Suranga Ruhunusiri⁶ , Laila Andersson⁴ , Christian Mazelle⁷ , and Shannon M. Curry¹ 

¹Space Sciences Laboratory, University of California, Berkeley, CA, USA, ²Department of Physics and Astronomy, West Virginia University, Morgantown, WV, USA, ³Goddard Space Flight Center, Greenbelt, MD, USA, ⁴Laboratory for Atmospheric and Space Physics, University of Colorado, Boulder, CO, USA, ⁵Department of Climate and Space Sciences and Engineering, University of Michigan, Ann Arbor, MI, USA, ⁶Department of Physics and Astronomy, University of Iowa, Iowa City, IA, USA, ⁷IRAP, CNRS - University of Toulouse - UPS - Centre national d'études spatiales (CNES), Toulouse, France

Abstract Discrete aurorae have been observed at Mars by multiple spacecraft, including Mars Express, Mars Atmosphere and Volatile EvolutionN (MAVEN), and most recently the United Arab Emirates Hope spacecraft. Meanwhile, there have been studies on the source particles responsible for producing these detectable aurorae (termed “auroral electrons”). By utilizing empirical criteria to select auroral electrons established by Xu et al. (2022, <https://doi.org/10.1029/2022GL097757>), we conduct statistical analyses of the impact of upstream drivers on the occurrence rate and fluxes of auroral electrons. We find the occurrence rate increases with upstream dynamic pressure and weakly depends on the interplanetary magnetic field strength. Meanwhile, the integrated auroral electron flux somewhat decreases with increasing upstream drivers. Auroral electron precipitation also occurs more frequently and is more intense over regions of strong crustal fields compared to weak crustal fields. Aside from emissions, auroral electrons are expected to cause significant impact ionization and enhance the plasma density locally. In this study, we also quantify the nightside ionospheric impact of auroral electron precipitation, specifically the thermal ion (O^+ , O_2^+ , and CO_2^+) density enhancement, with MAVEN observations. Our results show that the ion density is increased by up to an order of magnitude at low altitudes. The crustal effects on ion density profiles for nominal electron and auroral electron precipitation are also discussed.

Plain Language Summary Localized auroral emissions have been observed at Mars by multiple spacecraft, including Mars Express, Mars Atmosphere and Volatile EvolutionN (MAVEN), and most recently the United Arab Emirates Hope spacecraft. Meanwhile, there have been studies on the source particles responsible for producing these detectable aurorae, termed “auroral electrons.” By utilizing previously established criteria to select auroral electrons, we conduct statistical analyses of the impact of upstream drivers on the occurrence rate and also the intensity of auroral electrons. In the meantime, auroral emission is not the sole effect of electrons impacting the collisional atmosphere, but also an enhanced local ionization. Using both MAVEN observations, we show that the ion density is increased by up to an order of magnitude at low altitudes comparing auroral electron and nonauroral electron events.

1. Introduction

Discrete aurorae have been long observed at Earth's polar region (see review by Birn et al. (2012)) and more recently at Jupiter with observations from the Juno spacecraft (Mauk et al., 2017, 2020), both planets possessing an intrinsic global dipole field and a collisional atmosphere. Different types of aurorae are usually defined according to their particle sources and discrete aurorae are designated for auroral emission caused by accelerated electrons at these two planets, particularly broadband electron acceleration as a consequence of wave-particle interactions or inverted-V electron acceleration events. However, this phenomenon is not limited to magnetized planets but also observed at Mars, a planet with only localized strong crustal magnetic fields, by Mars express (Bertaux et al., 2005; Leblanc et al., 2006, 2008), Mars Atmosphere and Volatile EvolutionN (MAVEN) (e.g., Schneider et al., 2018, 2021), and most recently the United Arab Emirates' Hope spacecraft (Lillis et al., [2022, submitted to GRL, MS# 2022GL099820]).

At Mars, “discrete aurora” is defined more specifically for localized emissions, in contrast to global auroral emissions (Schneider et al., 2015). Several studies have associated these localized emissions with energized electron observations (Brain et al., 2006; Gérard et al., 2015; Leblanc et al., 2008; Soret et al., 2016, 2021; Xu et al., 2020, 2022). The reported energization processes/mechanisms at Mars include, but are not limited to, narrow electrostatic potential layers (associated with inverted-V electron events) (e.g., Brain et al., 2006; Xu et al., 2020), energization associated with current sheet crossings (e.g., Halekas et al., 2008; Harada et al., 2020), and a hotter electron temperature (without acceleration by an electrostatic potential) (Akbari et al., 2019) perhaps caused by wave-particle interaction (e.g., Fowler et al., 2020, 2021). Furthermore, it is speculated that the highly localized nature of Mars’s discrete auroral emission could also be a result of hotter upstream solar wind electrons during solar transient events precipitating onto localized regions due to Mars’s complex magnetic topology (Brain et al., 2007, 2020; Liemohn et al., 2007; Weber et al., 2017, 2020; Xu, Weber, et al., 2019). Therefore, to properly compare the discrete aurora phenomenon at Earth/Jupiter with that at Mars, we must have a better understanding of electron sources (nominal vs. hotter upstream solar wind electrons) and the energization mechanisms at Mars.

With mostly single-spacecraft observations at Mars, discrete auroral emissions and electron sources are usually observed separated in times and/or spatial locations. Xu et al. (2022) established empirical criteria to select electron events (termed “auroral electrons”) that can trigger detectable auroral emissions by the imaging ultraviolet spectrograph (IUVS) instrument (McClintock et al., 2015) onboard MAVEN by statistically comparing electron and auroral events. The selection criteria ensure that high-energy (~50–2,000 eV) electrons have sufficient fluxes and also access to the collisional atmosphere (more details provided in Section 2). A similar logic is adopted by Fang et al. (2022) to study the probability of auroral electrons with magnetohydrodynamic model results. By utilizing empirical criteria provided by Xu et al. (2022), we conduct a statistical analysis of the impact of upstream drivers on the occurrence rate and fluxes of auroral electrons. Such an analysis can not only be compared with the analysis of upstream drivers’ impact on discrete aurorae by Girazian et al. (2022) but also gives insight into the electron sources and energization mechanisms.

In the meantime, auroral emission is not the sole effect of electrons impacting the collisional atmosphere. It is expected for auroral electrons to cause significant ionization and enhance the plasma density locally. This is particularly important at Mars where the nightside ionosphere is patchy and significant contributions are made by electron impact ionization (Adams et al., 2018; Cui et al., 2019; Fillingim et al., 2007, 2010; Girazian et al., 2017; Lillis & Brain, 2013; Lillis et al., 2018; Withers, 2009). In this study, we will quantify the ionospheric impact, more specifically the thermal ion density enhancement, caused by these “extreme” (low occurrence rates and high fluxes) auroral electrons with MAVEN observations.

As described above, this study characterizes how the upstream drivers affect the occurrence rates and fluxes of auroral electrons as well as the impact on the Mars nightside ionosphere by their precipitation. This paper is organized as follows: The methodology section (Section 2) provides the descriptions of the selection criteria of auroral electrons, and how to obtain the upstream drivers and ion densities; the analysis of upstream driver effects is provided in Section 3 and the ionospheric impact in Section 4; we then discuss the results and conclude the paper in Section 5.

2. Methodology

To trigger detectable discrete aurorae, there are two necessities for source electrons (Fang et al., 2022; Xu et al., 2022). First, auroral electrons must have sufficient fluxes at an energy range of 50–2,000 eV (e.g., Soret et al., 2016, 2021) to produce CO Cameron band emission brightness above the instrument detection threshold (~0.5 kR for IUVS) with an emission altitude of 100–150 km. Second, auroral electrons must be on magnetic field lines connected to the nightside atmosphere, which naturally sets up a requirement of a one-sided loss cone pitch angle distribution. Such a pitch angle distribution is normally identified as an “open-to-night” topology (e.g., Brain et al., 2007, 2020; Weber et al., 2017, 2020; Xu, Curry, et al., 2019) but the actual magnetic topology might be open or closed in the presence of parallel electric fields. More specifically, Xu et al. (2022) provide the following criteria to select auroral electrons:

1. The integrated electron energy flux over 50–2,000 eV to be $>1.1 \times 10^{10} \text{ eV cm}^{-2}\text{s}^{-1}\text{sr}^{-1}$ (or $0.018 \text{ mW m}^{-2} \text{sr}^{-1}$);
2. An “open-to-night” topology (one-sided loss cone pitch angle distributions).

We select auroral electron events by applying these criteria to suprathermal electron measurements by the Solar Wind Electron Analyzer (SWEA) (Mitchell et al., 2016) from 1 December 2014 to 1 April 2020, limited to solar zenith angle (SZA) $>95^\circ$ (following Xu et al. (2022)) and an altitude range of 150–500 km. One-sided loss cone distributions are selected by comparing upward and downward electron fluxes to perpendicular electron fluxes within 100–300 eV (Weber et al., 2017; Xu, Weber, et al., 2019). Following Xu et al. (2022), three occurrence rates can be calculated: $O_e = N_e/N_{\text{tot}}$ for the overall occurrence rate of auroral electrons, $O_t = N_t/N_{\text{tot}}$ for the occurrence rate of the open-to-night topology, and $O_{et} = N_e/N_t$ for the occurrence rate of auroral electron events on the open-to-night topology alone, where N_e , N_t , and N_{tot} are the sample number of auroral electron observations, the sample number of the open-to-night topology, and the sample number of all (auroral and nonauroral) electron observations, respectively. We also examine the variation in the integrated electron energy flux over 50–2,000 eV (I_e in units of $\text{eV cm}^{-2}\text{s}^{-1}\text{sr}^{-1}$ or $\text{mW m}^{-2}\text{sr}^{-1}$) and the energy of peak energy fluxes (E_p) of auroral electron events.

To investigate the effects of upstream drivers, we utilize upstream solar wind density and velocity measured by the Solar Wind Ion Analyzer instrument (Halekas et al., 2015). For upstream interplanetary magnetic field (IMF), we use the measured magnetic vectors by the Magnetometer (Connerney et al., 2015) when MAVEN samples the upstream solar wind (Halekas et al., 2017) but otherwise use a proxy provided by Ruhunusiri et al. (2018). Upstream drivers are orbit averages given at apoapsis times, one set per orbit, and are thus linearly interpolated to local measurements based on time. To characterize the ionospheric impact, we examine the densities of main planetary ions, O^+ , O_2^+ , and CO_2^+ , measured by the SupraThermal And Thermal Ion Composition (STATIC) instrument (McFadden et al., 2015). More specifically, Fowler et al. (2022) provide the detailed description of all the necessary calibrations to calculate these ion densities.

3. Upstream Drivers

In this section, we focus on auroral electron events only and examine both the occurrence rates and integrated energy fluxes (I_e) of auroral electrons as a function of upstream parameters to characterize their impact on auroral electrons at Mars. We also separately study these impacts for strong ($|B_{r170}| > 30$ nT) and weak ($|B_{r170}| < 5$ nT) crustal magnetic fields, where $|B_{r170}|$ is the modeled radial crustal field strength at 170 km (Morschhauser et al., 2014) and radially mapped to the spacecraft location based on its latitude and longitude. Radial crustal fields are used following previous studies (Girazian et al., 2022; Schneider et al., 2021; Xu et al., 2022).

3.1. Occurrence Rates

Figure 1 displays the occurrence rate of auroral electrons (O_e) as a function of upstream solar wind velocity (V_{SW}) and density (n_{SW}) (left column) and as a function of upstream solar wind dynamic pressure (P_{dyn}) and IMF strength ($|B_{\text{imf}}|$) (right column), separately for all regions (a–b), weak (c–d) and strong (e–f) crustal magnetic fields. As shown in the left column, O_e generally increases from <0.001 to >0.01 , more than one order of magnitude, with increasing V_{SW} and n_{SW} . O_e is also well organized by dynamic pressure levels, as indicated by the dashed lines in the left column. O_e over weak crustal fields (c) varies similarly as panel (a) with V_{SW} and n_{SW} , consequently P_{dyn} . In contrast, over strong crustal fields, Figure 1e shows O_e is higher (~ 0.003) at low P_{dyn} and then increases to a value (~ 0.05) similar to that of the weak crustal fields at high P_{dyn} . In other words, P_{dyn} has a stronger effect on O_e over weak crustal fields than over strong crustal fields. As upstream drivers are somewhat correlated, we plot O_e against P_{dyn} and $|B_{\text{imf}}|$ in the right column to examine their effect separately. This again shows O_e mainly increases with P_{dyn} . In comparison, the increase in O_e with $|B_{\text{imf}}|$ is less apparent until $|B_{\text{imf}}| > \sim 5$ nT.

Figure 2 shows the occurrence rate of the open-to-night topology (O_t) as a function of different drivers in the same format as Figure 1 but the color scale is linear. In the left column of Figure 2, O_t increases with V_{SW} and n_{SW} but only from ~ 0.075 to ~ 0.3 , varying by a factor of a few. Similarly, P_{dyn} organizes O_t reasonably well. In the right column of Figure 2, $|B_{\text{imf}}|$ has a mild impact on O_t over weak crustal fields (d), especially at high IMF strengths, and arguably over strong crustal fields too (f).

As shown in Figure 3, the occurrence rate of auroral electrons on “open-to-night” topology only (O_{et}) behaves similarly to O_e (Figure 1) in response to upstream drivers. The left column of Figure 3 shows O_{et} increases significantly with V_{SW} , n_{SW} , and thus P_{dyn} , about an order of magnitude for all data (a) and over weak crustal fields (c) but only a factor of a few over strong crustal fields (e). Similarly, O_{et} increases more with $|B_{\text{imf}}|$, particularly for

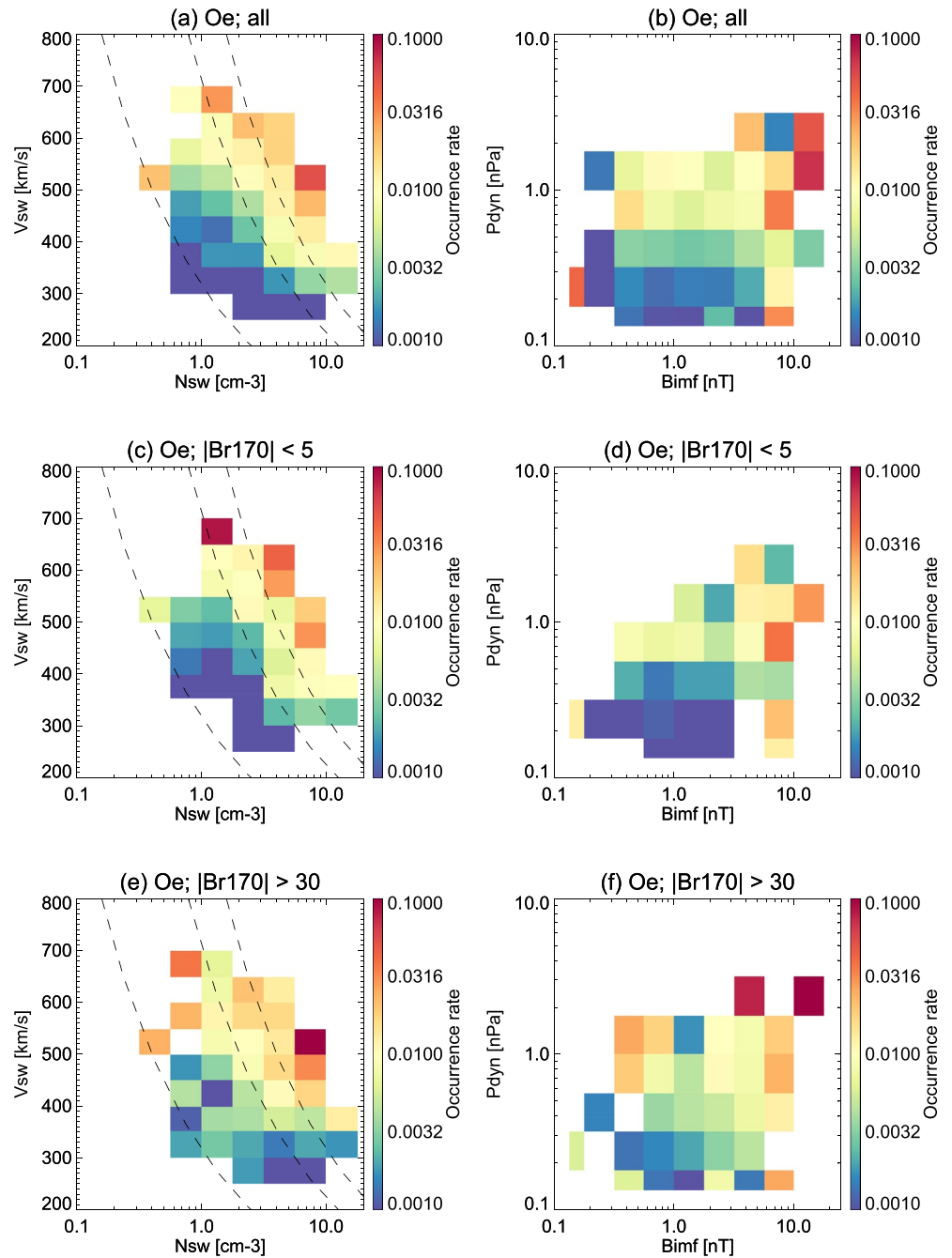


Figure 1. The occurrence rate of auroral electrons (O_e) as a function of upstream solar wind velocity and density (left column) and as a function of upstream solar wind dynamic pressure and interplanetary magnetic field strength (right column). The top row (a–b) is based on all the data; the middle row (c–d) is limited to weak crustal magnetic fields ($|B_{r170}| < 5$ nT); and the bottom row is limited to strong magnetic crustal fields ($|B_{r170}| > 30$ nT). $|B_{r170}|$ is the modeled radial crustal field strength at 170 km (Morschhauser et al., 2014). The three dashed lines in the left column, from left to right, mark equal dynamic pressures of 0.1 nPa, 0.5 nPa, and 1 nPa, respectively.

$|B_{imf}| > \sim 5$ nT, for all data (b) and over weak crustal fields (d). The increase in O_{et} with respect to $|B_{imf}|$ is less prominent over strong crustal fields (f).

To summarize, Figures 1–3 show similar trends: (a) O_e , O_p , and O_{et} increase systematically with increasing P_{dyn} (corresponding to an increase in V_{SW} and/or n_{SW}); (b) $|B_{imf}|$ has a milder impact on these occurrence rates, compared to P_{dyn} ; (c) the increase in O_{et} with drivers is more prominent than the increase in O_p ; and (d) the

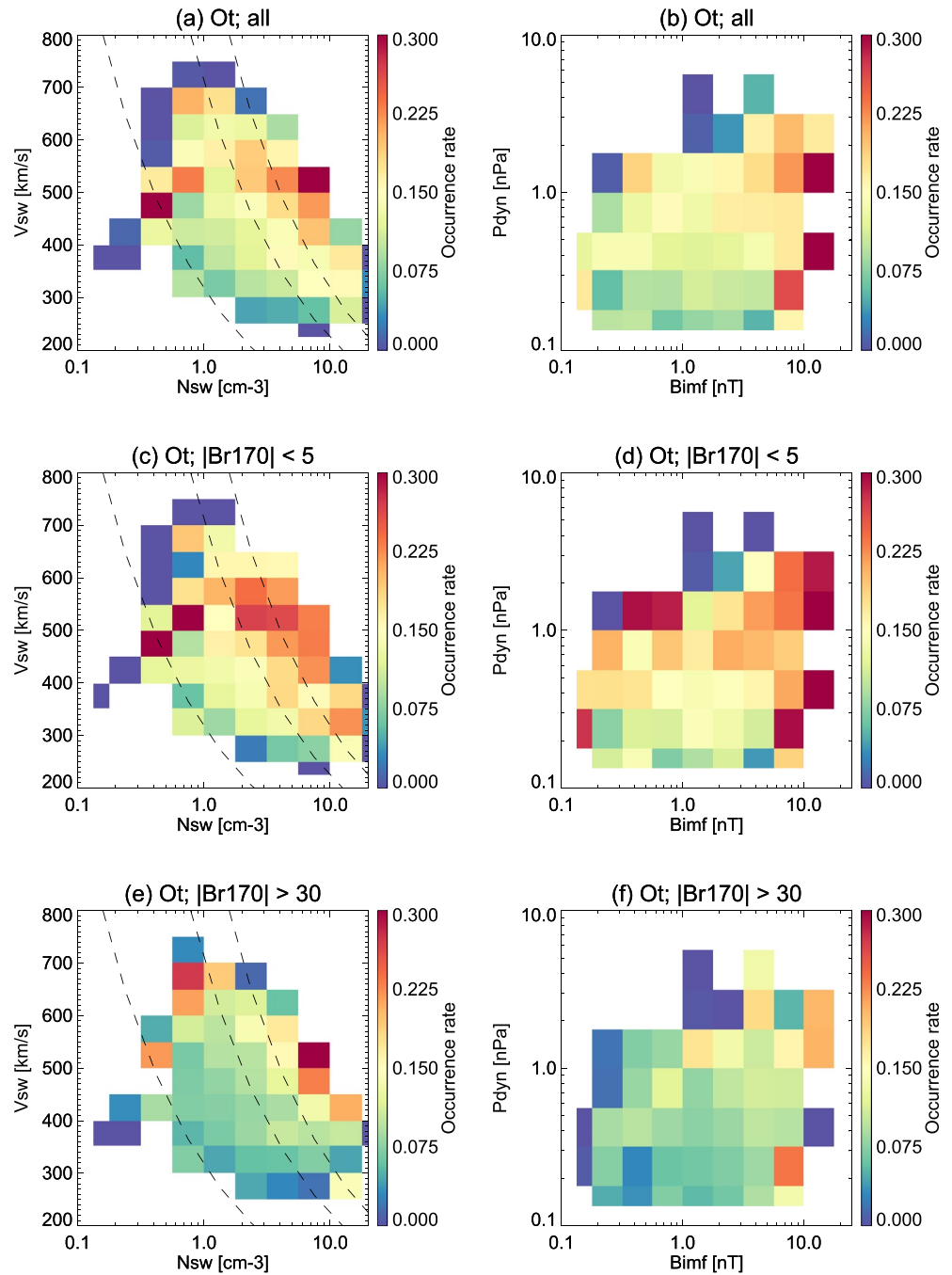


Figure 2. The same format as Figure 1 but for the occurrence rate of the “open-to-night” topology (O_t). Note that the color scale for O_t is linear.

increase in occurrence rates with varying upstream drivers is more prominent over weak crustal fields than that over strong crustal fields.

3.2. Electron Fluxes and Peak Energies

In this section, we examine how the integrated electron fluxes (I_e , $\text{eV cm}^{-2}\text{s}^{-1}\text{sr}^{-1}$) for selected auroral electrons change with upstream drivers. Figure 4 illustrates I_e as a function of n_{sw} , V_{sw} , P_{dyn} , and $|B_{\text{imf}}|$, in the same format as Figures 1–3. The left column shows that I_e has a moderate decrease (within a factor of 2–3) with increasing

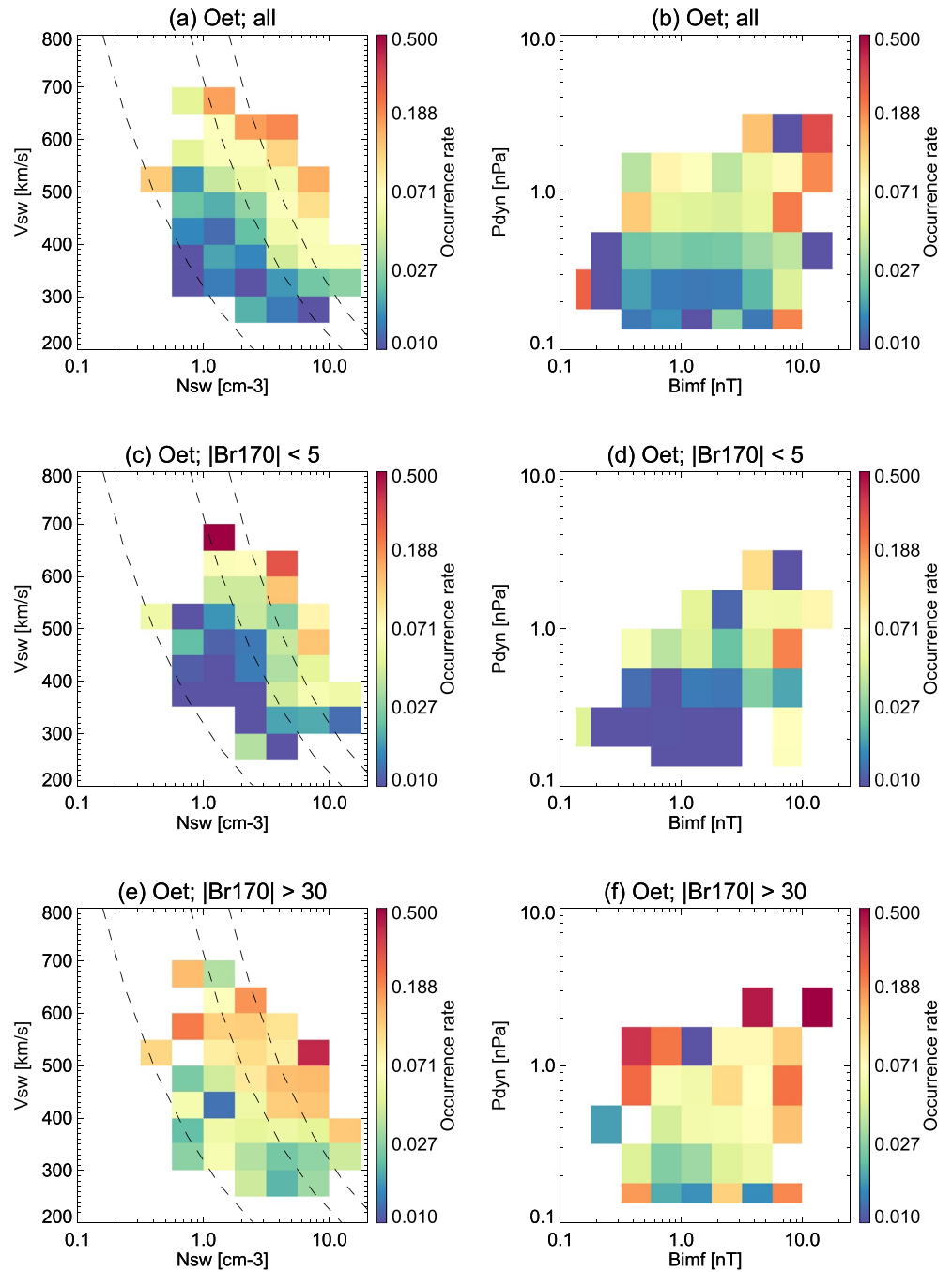


Figure 3. The same format as Figure 1 but for the occurrence rate of auroral electrons on “open-to-night” topology only (O_{et}).

n_{sw} , V_{sw} , and thus P_{dyn} , less prominent over weak crustal fields (c). The right column shows that I_e is somewhat insensitive to $|B_{imf}|$. As our selection threshold for I_e is $1.1 \times 10^{10} \text{ eV cm}^{-2}\text{s}^{-1}\text{sr}^{-1}$, the median I_e under large dynamic pressures ($> \sim 0.5 \text{ nPa}$) has values very close to the threshold while I_e is significantly higher than the threshold during low dynamic pressures ($< \sim 0.5 \text{ nPa}$). Girazian et al. (2022) reported that the discrete auroral brightness is insensitive to the dynamic pressure, which is roughly consistent with the relatively small change in median I_e in Figure 4.

It is interesting that at large P_{dyn} and $|B_{imf}|$, the occurrence rates (O_e , O_r , and O_{et}) generally increase while the median I_e decreases. This implies that even though it is more likely for auroral electrons to occur during strong

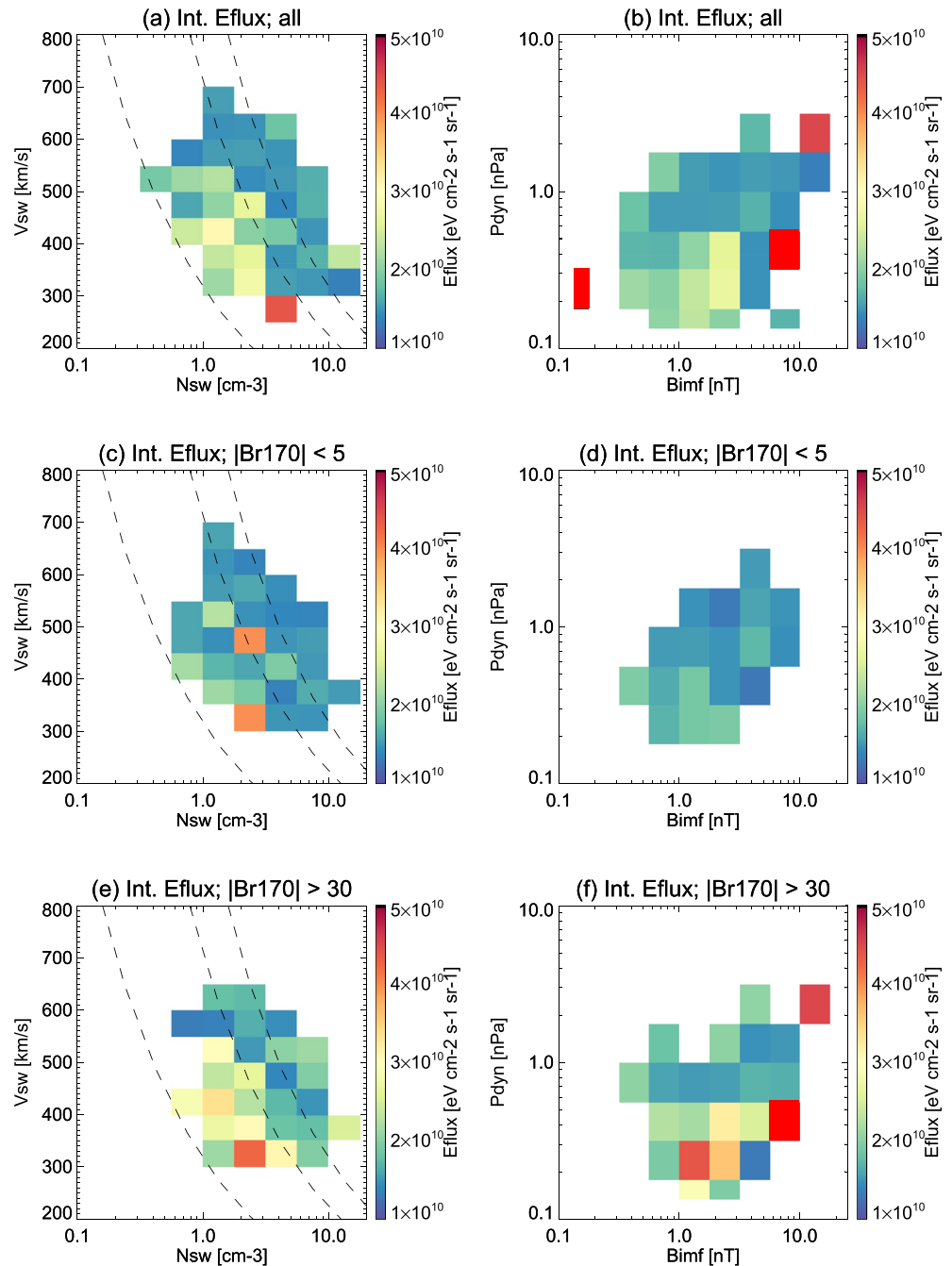


Figure 4. The same format as Figure 1 but for the median integrated electron fluxes (I_e , $\text{eV cm}^{-2}\text{s}^{-1}\text{sr}^{-1}$) of auroral electron events only. Note that the color scale for I_e is linear.

driver periods, these auroral electrons tend to have smaller fluxes. To understand it further, we plot the median peak energy (for maximum energy flux) of auroral electron events as a function of different drivers in Figure 5, in the same format as Figure 1. The peak energy (E_p) decreases from above 100 to ~ 50 eV with increasing n_{sw} (a, c, and e), V_{sw} (a, c, and e), P_{dyn} (b, d, and f), and arguably $|B_{\text{imf}}|$ (b, d, and f) too. The peak energy is also generally lower over weak crustal fields than over strong crustal fields, except for at highest driver periods comparing panels c–d to panels e–f. These trends suggest electrons are less accelerated (a) over weak crustal fields than over strong crustal fields and (b) during high driver periods than during low driver periods. We will discuss the implications of these statistical trends in Section 5.

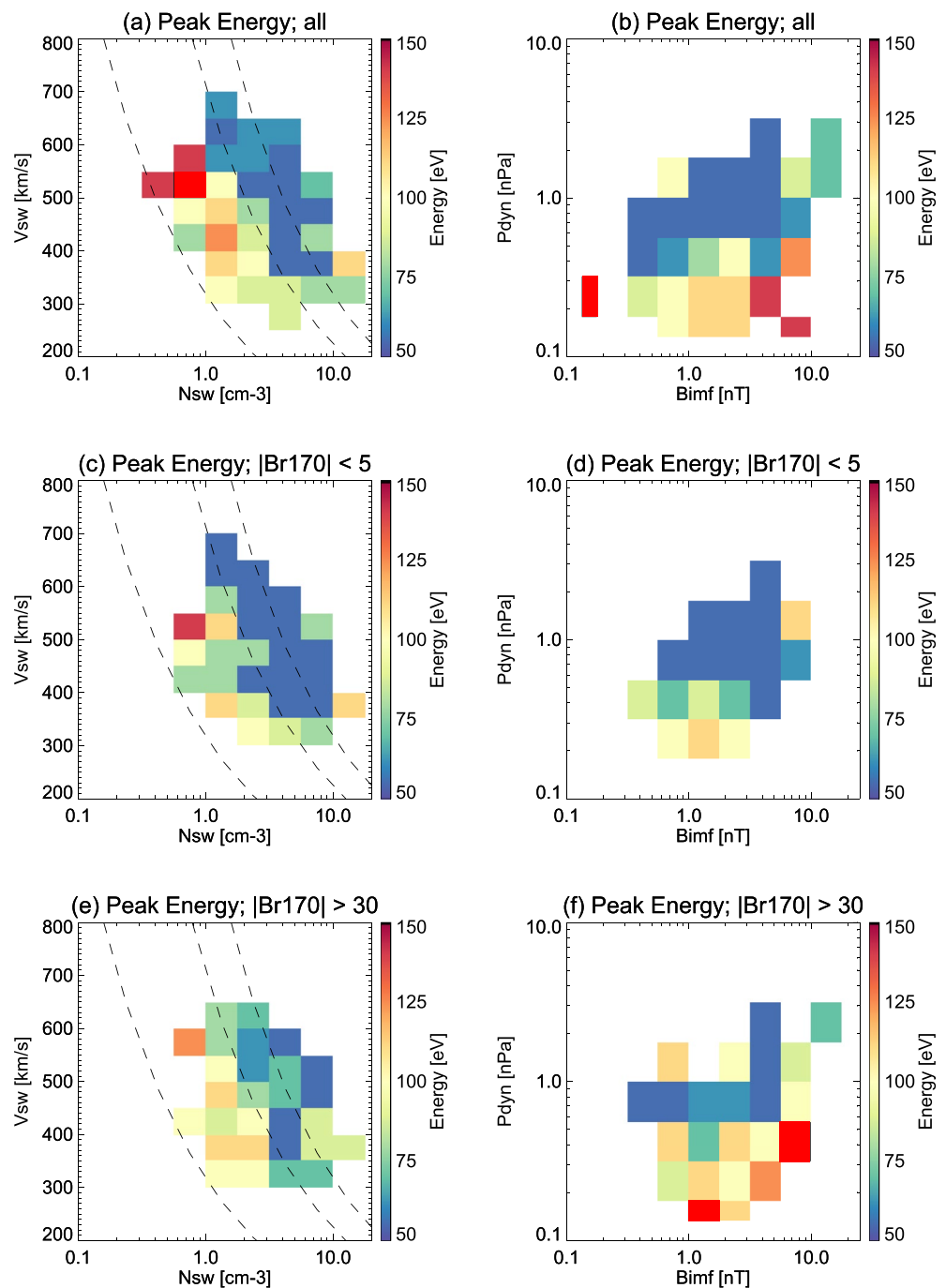


Figure 5. The same format as Figure 1 but for median peak energy (for maximum energy flux) of auroral electron events.

4. Ionospheric Impact

As mentioned previously, electron precipitation is an important source of the Mars nightside ionosphere. In this section, we quantify the impact of auroral electrons on the density profiles of different ion species, measured by the STATIC instrument. We limit the data to $SZA > 110^\circ$, above which ion densities have little SZA dependence (Fowler et al., 2022). We compare the density profiles for auroral electron events and nominal electron events, defined as I_e above and below the flux threshold of $1.1 \times 10^{10} \text{ eV cm}^{-2}\text{s}^{-1}\text{sr}^{-1}$, respectively. In addition, we only examine cases with open-to-night topology such that the main variability is the intensity of precipitating electrons, as other drivers, such as thermospheric density changes and ion winds, are contained in both nominal and

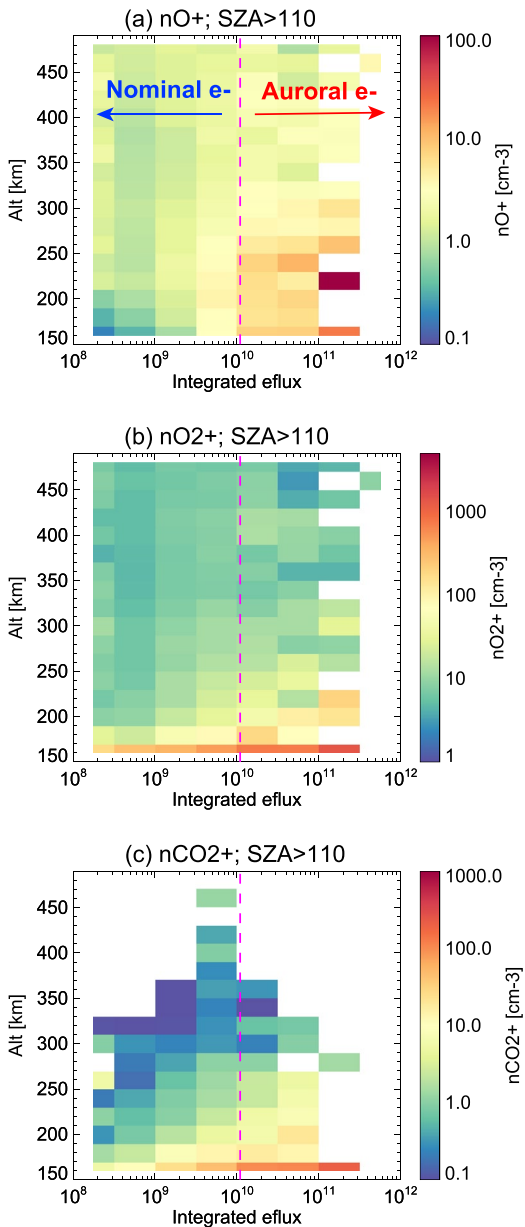


Figure 6. Median ion densities as a function of integrated electron energy fluxes I_e ($\text{eV cm}^{-2}\text{s}^{-1}\text{sr}^{-1}$) and altitude, (a) for O^+ , (b) for O_2^+ , and (c) for CO_2^+ . The dashed magenta lines mark the electron flux threshold separating nominal electrons and auroral electrons.

auroral electron cases. It is worth noting that Girazian et al. (2017) evaluated how ion densities vary for high and low ionizing electron fluxes with ion measurements from the Neutral Gas and Ion Mass Spectrometer (NGIMS) onboard MAVEN, but not discerning magnetic topology. The NGIMS instrument has a small field of view (FOV) and might thus miss a portion of ions on the nightside due to plasma transport above $\sim 200\text{--}300$ km altitude. In comparison, STATIC has a much broader FOV but provides measurements of limited ion species. In addition, we limit to cases where superthermal electrons have access to the collisional atmosphere (open-to-night topology) and focus on the impact of “extreme” (low occurrence rates and high fluxes) auroral electron precipitation events.

Figure 6 shows the median ion densities as a function of I_e and altitude, (a) for O^+ , (b) for O_2^+ , and (c) for CO_2^+ . For all species, ion densities increase as I_e increases up to an order of magnitude, particularly at low altitudes. In addition, $n(O^+)$ normally has a peak altitude of ~ 250 km, evident in panel (a) for small I_e and is enhanced significantly below 300 km altitude for large I_e . In contrast, the peak altitudes for $n(O_2^+)$ and $n(CO_2^+)$ are located nominally at $< \sim 160$ km on the nightside, at or below the nominal MAVEN periapsis altitude, such that we do not observe similar changes in the peak altitude as O^+ . Similar density enhancements and the change in O^+ density peak altitude comparing low and high ionizing electron fluxes are also reported by Girazian et al. (2017).

To more quantitatively compare cases with nominal electron precipitation and auroral electron precipitation, Figure 7 displays the ion densities as a function of altitude separated for I_e above (red) and below (blue) 1.1×10^{10} $\text{eV cm}^{-2}\text{s}^{-1}\text{sr}^{-1}$, (a) for O^+ , (b) for O_2^+ , and (c) for CO_2^+ , and the ratios of median ion densities of the two scenarios in (d). In general, the density enhancement is within a factor of 2 above 300 km altitude for all ion species and by a larger factor below, up to a factor of 6 for $n(O_2^+)$ (magenta line) and $n(CO_2^+)$ (green line), and a factor of 12 for $n(O^+)$ (black line), as shown in panel d. In short, an increase in ion densities because of the precipitation of auroral electrons is seen across all ion species at lower altitudes (closer to the production region), by a larger factor for O^+ and a smaller factor for O_2^+ and CO_2^+ . This is mainly because the peak altitude of O^+ is shifted to lower altitudes as auroral electrons tend to be more energetic.

Over weak crustal fields, ion density profiles and density ratios for nominal electron precipitation and auroral electron precipitation are illustrated in Figure 8, in the same format as Figure 7. In Figures 8a and 8d, the density ratio of O^+ generally increases with decreasing altitude with a peak factor of 8 at ~ 200 km. In Figures 8b and 8d, the density enhancement of O_2^+ also increases with decreasing altitude, from less than a factor of 2 above 250 km to up to a factor of 5 at 150 km. In Figures 8c and 8d, there are only sufficient measurements of CO_2^+ below 200 km for $I_e > 1.1 \times 10^{10}$ $\text{eV cm}^{-2}\text{s}^{-1}\text{sr}^{-1}$ with a density ratio of 2–4.

Similarly, Figure 9 illustrates ion density profiles and density ratios for nominal electron precipitation and auroral electron precipitation over strong crustal fields. In panels a and d, the density ratio of O^+ is a factor of 2–8.5, peaking at 150 km altitude. In panels b and d, the enhancement in $n(O_2^+)$ is not so obvious, within a factor 3. In panels c and d, the density ratio of CO_2^+ increases with decreasing altitude, from equity at 300 km to a maximum value of 6.5 at 150 km.

Comparing weak and strong crustal fields for nominal electron precipitation (blue lines in Figures 8a–8c and 9a–c), ion densities over strong crustal fields are generally higher than those over weak crustal fields,

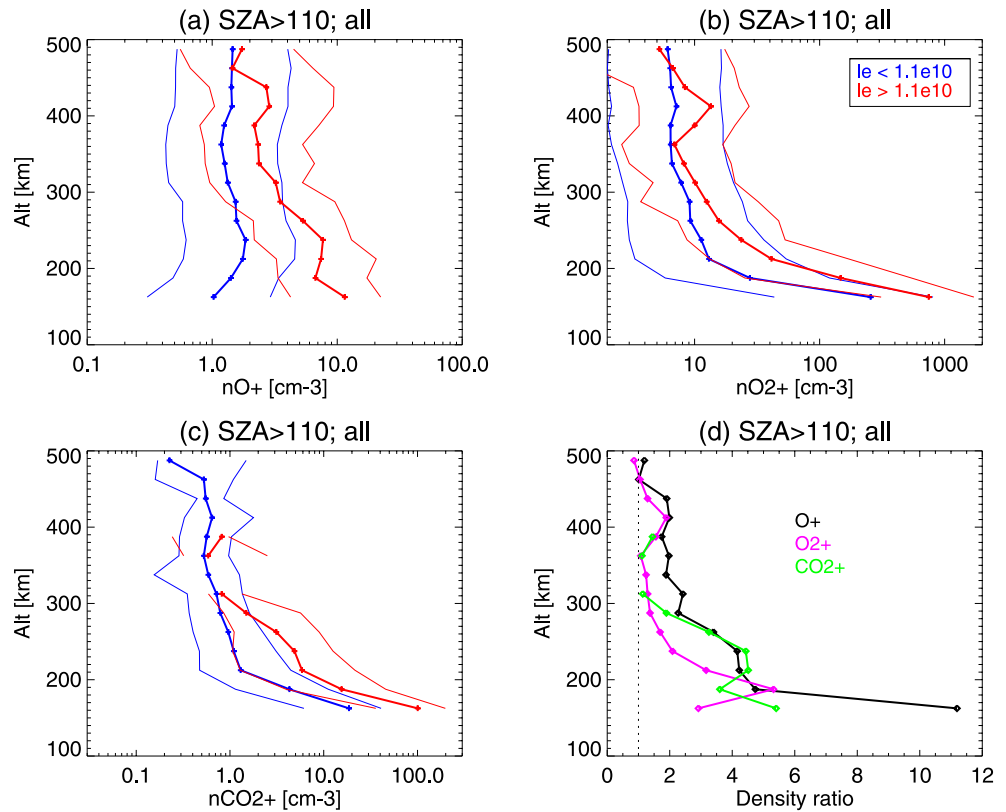


Figure 7. (a–c) Median ion densities (thick lines, with thin lines as quartiles) as a function of altitude separated for integrated electron energy fluxes above (red) and below (blue) $1.1 \times 10^{10} \text{ eV cm}^{-2} \text{ s}^{-1} \text{ sr}^{-1}$, (a) for O^+ , (b) for O_2^+ , and (c) for CO_2^+ . (d) The ratio between median ion densities measured when integrated electron fluxes are above and below $1.1 \times 10^{10} \text{ eV cm}^{-2} \text{ s}^{-1} \text{ sr}^{-1}$, different colors for different ion species.

especially for O_2^+ and CO_2^+ below ~ 300 km altitude. In fact, a steeper density decrease, implying a smaller ion scale height, is seen in O_2^+ and CO_2^+ from 150 to 200 km altitude over weak crustal fields (Figures 8b and 8c) than that of strong crustal fields (Figures 9b and 9c). This implies that the vertical plasma diffusion is more efficient from the main peak to higher altitudes over strong crustal fields. Comparing weak and strong crustal fields for auroral electron precipitations (red lines in Figures 8a–8c and 9a–c), both $n(O^+)$ and $n(O_2^+)$ have similar profiles for two regions below ~ 300 km altitude but $n(O^+)$ seems to have a more vertically extended density peak over strong crustal fields. In contrast, $n(CO_2^+)$ is much higher over strong crustal fields than that of weak crustal fields below 200 km altitude. These features could be explained by the following reasons: Over strong crustal fields, (a) a higher I_e (Figures 4c–4f) resulting in a higher production rate; (b) more local acceleration events with higher electron peak energies (Figures 5c–5f) that penetrate deeper into the atmosphere; and (c) a more effective vertical plasma diffusion. In addition, the chemical lifetimes of CO_2^+ and O^+ are shorter than O_2^+ ion species such that the densities of CO_2^+ and O^+ reflects more directly on the immediate local production.

5. Discussion and Conclusions

Discrete aurora and its source electrons have both been observed and studied at Mars. Building on Xu et al. (2022), we apply the same selection criteria to identify auroral electrons and determine how the upstream drivers affect their occurrence rates and also the integrated electron fluxes. Furthermore, auroral electron impact can cause effects other than observable auroral emission, one of which is the enhanced local ionization and thus local ion densities. We quantify the ion (O^+ , O_2^+ , and CO_2^+) density enhancement with MAVEN STATIC observations.

Our results indicate that the occurrence rates of auroral electrons (O_e), of open-to-night topology (O_t), and of auroral electrons on open-to-night topology (O_{et}) are well organized by upstream dynamic pressure (P_{dyn}), and only weakly depend on upstream IMF strength ($|B_{imf}|$). The increase in O_{et} with drivers is more prominent than

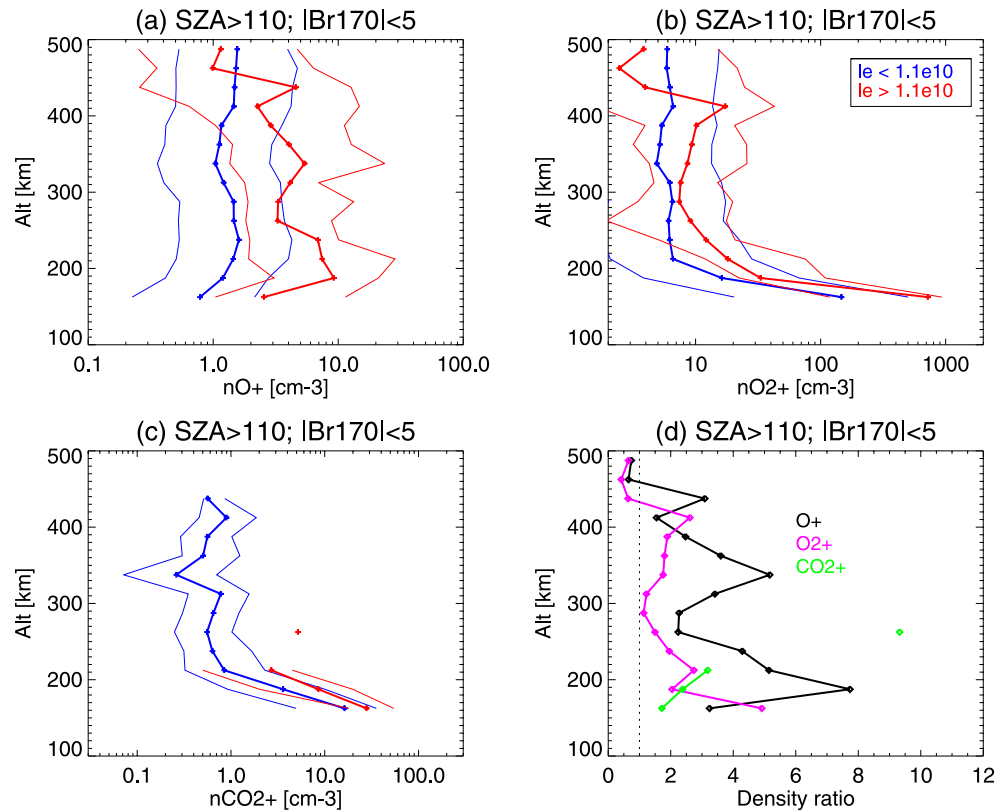


Figure 8. The same format as Figure 7 but limited to weak crustal magnetic fields ($|B_{r170}| < 5$ nT).

that of O_e . This suggests that while the magnetosphere becomes more open during more disturbed upstream conditions (e.g., Luhmann et al., 2017; Xu, Curry, et al., 2019; Xu et al., 2018; Weber et al., 2019, 2020), the increase in O_e is mainly because the mechanisms responsible for enhanced high-energy electron fluxes operate more often during high P_{dyn} and/or high $|B_{\text{imf}}|$. Meanwhile, the integrated electron flux (I_e) for auroral electron events somewhat decreases with P_{dyn} but less so with $|B_{\text{imf}}|$. Girazian et al. (2022) reported a generally increased occurrence rate of discrete aurorae with increasing P_{dyn} but little response to $|B_{\text{imf}}|$, with the auroral brightness insensitive to P_{dyn} (with a slightly lower brightness at high P_{dyn}). This is consistent with our reported trends of O_e and I_e with respect to upstream drivers.

To investigate the cause of opposite trends in occurrence rates and electron intensities with respect to upstream drivers, we further examine the peak energy (E_p) of auroral electron events, which decreases with increasing n_{sw} , V_{sw} , and P_{dyn} , arguably $|B_{\text{imf}}|$ too. These trends combined show that the increase in the driver intensity does not necessarily cause more intense electron precipitation events but rather that under stronger drivers, there are more auroral electron events just surpassing our electron flux threshold. One possible explanation is that during high driver periods, upstream solar wind electrons tend to be hotter and denser than that during quiet times such that a smaller energization (or maybe no energization at all) is needed to exceed the electron flux threshold. This would explain the decrease in E_p with increasing driver values. In addition, larger energizations tend to occur less frequently. This would then explain the occurrence rates of auroral electrons (O_e and O_{ct}) are much lower during low driver periods (larger energization needed) than high driver periods (smaller energization needed).

Comparing strong ($|B_{r170}| > 30$ nT) and weak crustal fields ($|B_{r170}| < 5$ nT), electron occurrence rates, median I_e , and median E_p are lower over weak crustal fields than over strong crustal fields during low driver periods but become similar during high driver periods for both regions. A possible explanation might be that electron energizations are less intense over weak crustal fields (smaller E_p during low driver periods) than over strong crustal fields. Then, during high driver periods, smaller energizations are needed to meet the electron flux selection criterion, making auroral electron events having similar statistical properties for both strong and weak crustal fields.

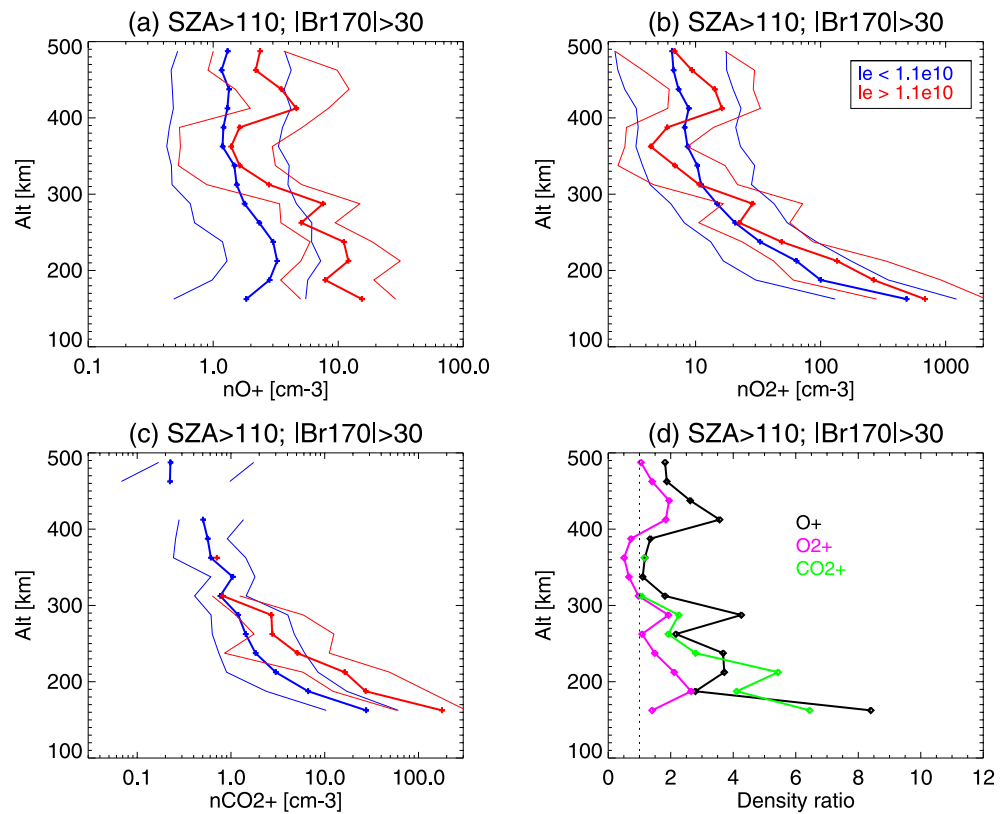


Figure 9. The same format as Figure 7 but limited to strong crustal magnetic fields ($|B_{r170}| > 30$ nT).

As electron precipitation is an important source to maintain the nightside ionosphere, we observe a corresponding increase in O^+ , O_2^+ , and CO_2^+ densities with increasing integrated electron fluxes (I_e). More specifically, we examine the median density profiles for nominal electron ($I_e < 1.1 \times 10^{10}$ eV cm⁻²s⁻¹sr⁻¹) and auroral electron ($I_e > 1.1 \times 10^{10}$ eV cm⁻²s⁻¹sr⁻¹) precipitation. The density enhancement is up to an order of magnitude on average and mainly occurs below 300 km altitude, close to the main production region. The enhancement is more prominent in O^+ and CO_2^+ densities at low altitudes because the chemical lifetimes of these two ion species are shorter and, thus, their densities are more responsive to enhanced electron precipitation. Comparing strong and weak crustal fields, the ion density profiles show similarities and differences for nominal electron and auroral electron precipitation, which could probably be explained by some combinations of the following reasons: over strong crustal fields, a higher I_e resulting in a higher production rate, more local acceleration events with higher electron peak energies that penetrate deeper into the atmosphere, and/or a more effective vertical plasma diffusion.

To summarize, this study provides a statistical analysis of how the upstream drivers affect auroral electrons at Mars, which helps explain the behavior of discrete aurora in response to upstream drivers and also gives insights into the electron sources and energization mechanisms at Mars. Meanwhile, the precipitation of auroral electrons can cause enhanced ionization. This study also provides a characterization of local ionospheric disturbances to the nightside ionosphere produced by auroral electron precipitation. In short, our study advances the current understanding of the causes and effects of auroral electrons at Mars and lays the ground for comparative studies of discrete aurora at different planets.

Data Availability Statement

The MAVEN data used in this study are available through the Planetary Data System (<https://pds-ppi.igpp.ucla.edu/mission/MAVEN>).

Acknowledgments

This work was supported by the National Aeronautics and Space Administration (NASA) grant NNH10CC04C to the University of Colorado and by subcontract to Space Sciences Laboratory, University of California, Berkeley. The MAVEN project is supported by NASA through the Mars Exploration Program. S. Xu, S. M. Curry, and D. L. Mitchell also acknowledge support from NASA's Mars Data Analysis Program, grant 80NSSC17K0455. Parts of this work for the observations obtained with the SWEA instrument are supported by the French space agency CNES (National Centre for Space Studies).

References

Adams, D., Xu, S., Mitchell, D. L., Lillis, R. L., Fillingim, M., Andersson, L., et al. (2018). Using magnetic topology to probe the sources of Mars' nightside ionosphere. *Geophysical Research Letters*, *45*(22), 12190–12197. <https://doi.org/10.1029/2018gl080629>

Akbari, H., Andersson, L., Fowler, C., & Mitchell, D. (2019). Spectral analysis of accelerated electron populations at Mars. *Journal of Geophysical Research: Space Physics*, *124*, 8056–8065. <https://doi.org/10.1029/2019ja026738>

Bertaux, J.-L., Leblanc, F., Witasse, O., Quemerais, E., Liliensten, J., Stern, S., et al. (2005). Discovery of an aurora on Mars. *Nature*, *435*(7043), 790–794. <https://doi.org/10.1038/nature03603>

Birn, J., Artemyev, A., Baker, D., Echim, M., Hoshino, M., & Zelenyi, L. (2012). Particle acceleration in the magnetotail and aurora. *Space Science Reviews*, *173*(1–4), 49–102. <https://doi.org/10.1007/s11214-012-9874-4>

Brain, D., Halekas, J., Peticolas, L., Lin, R., Luhmann, J., Mitchell, D., et al. (2006). On the origin of aurora on Mars. *Geophysical Research Letters*, *33*(1), L01201. <https://doi.org/10.1029/2005gl024782>

Brain, D., Lillis, R., Mitchell, D., Halekas, J., & Lin, R. (2007). Electron pitch angle distributions as indicators of magnetic field topology near Mars. *Journal of Geophysical Research*, *112*. <https://doi.org/10.1029/2007ja012435>

Brain, D., Weber, T., Xu, S., Mitchell, D. L., Lillis, R. J., Halekas, J. S., et al. (2020). Variations in nightside magnetic field topology at Mars. *Geophysical Research Letters*, *47*(19), e2020GL088921. <https://doi.org/10.1029/2020gl088921>

Connerney, J., Espley, J., Lawton, P., Murphy, S., Odom, J., Oliverson, R., & Sheppard, D. (2015). The MAVEN magnetic field investigation. *Space Science Reviews*, *195*(1–4), 1–35. <https://doi.org/10.1007/s11214-015-0169-4>

Cui, J., Cao, Y.-T., Wu, X.-S., Xu, S.-S., Yelle, R., Stone, S., et al. (2019). Evaluating local ionization balance in the nightside Martian upper atmosphere during maven deep dip campaigns. *The Astrophysical Journal Letters*, *876*(1), L12. <https://doi.org/10.3847/2041-8213/ab1b34>

Fang, X., Ma, Y., Schneider, N., Girazian, Z., Luhmann, J., Milby, Z., et al. (2022). Discrete Aurora on the nightside of Mars: Occurrence location and probability. *Journal of Geophysical Research: Space Physics*, *127*. <https://doi.org/10.1029/2021JA029716>

Fillingim, M., Peticolas, L., Lillis, R., Brain, D., Halekas, J., Lummerzheim, D., & Bougher, S. (2010). Localized ionization patches in the nighttime ionosphere of Mars and their electrodynamic consequences. *Icarus*, *206*(1), 112–119. <https://doi.org/10.1016/j.icarus.2009.03.005>

Fillingim, M. O., Peticolas, L. M., Lillis, R. J., Brain, D. A., Halekas, J. S., Mitchell, D. L., et al. (2007). Model calculations of electron precipitation induced ionization patches on the nightside of Mars. *Geophysical Research Letters*, *34*(12), 12101. <https://doi.org/10.1029/2007GL029986>

Fowler, C. M., Agapitov, O. V., Xu, S., Mitchell, D. L., Andersson, L., Artemyev, A., et al. (2020). Localized heating of the Martian topside ionosphere through the combined effects of magnetic pumping by large-scale magnetosonic waves and pitch angle diffusion by whistler waves. *Geophysical Research Letters*, *47*(5), e2019GL086408. <https://doi.org/10.1029/2019GL086408>

Fowler, C. M., Hanley, K. G., McFadden, J. P., Chaston, C. C., Bonnell, J. W., Halekas, J. S., et al. (2021). MAVEN observations of low frequency steepened magnetosonic waves and associated heating of the Martian nightside ionosphere. *Journal of Geophysical Research: Space Physics*, *126*, e2021JA029615. <https://doi.org/10.1029/2021JA029615>

Fowler, C. M., McFadden, J., Hanley, K., Mitchell, D. L., Curry, S., & Jakosky, B. (2022). In-situ measurements of ion density in the Martian ionosphere: Underlying structure and variability observed by the MAVEN-STATIC instrument. *Journal of Geophysical Research: Space Physics*, *127*, e2022JA030352. <https://doi.org/10.1029/2022JA030352>

Gérard, J.-C., Soret, L., Libert, L., Lundin, R., Stiepen, A., Radioti, A., & Bertaux, J.-L. (2015). Concurrent observations of ultraviolet aurora and energetic electron precipitation with Mars Express. *Journal of Geophysical Research: Space Physics*, *120*, 6749–6765. <https://doi.org/10.1002/2015ja021150>

Girazian, Z., Mahaffy, P., Lillis, R. J., Benna, M., Elrod, M., Fowler, C. M., & Mitchell, D. L. (2017). Ion densities in the nightside ionosphere of Mars: Effects of electron impact ionization. *Geophysical Research Letters*, *44*(22), 11248–11256. <https://doi.org/10.1002/2017GL075431>

Girazian, Z., Schneider, N. M., Milby, Z., Fang, X., Halekas, J., Weber, T., et al. (2022). Discrete aurora at Mars: Dependence on upstream solar wind conditions. *Journal of Geophysical Research: Space Physics*, *127*, e2021JA030238. <https://doi.org/10.1029/2021JA030238>

Halekas, J., Brain, D., Lin, R., Luhmann, J., & Mitchell, D. (2008). Distribution and variability of accelerated electrons at Mars. *Advances in Space Research*, *41*(9), 1347–1352. <https://doi.org/10.1016/j.asr.2007.01.034>

Halekas, J., Ruhunusiri, S., Harada, Y., Collinson, G., Mitchell, D., Mazelle, C., et al. (2017). Structure, dynamics, and seasonal variability of the Mars-solar wind interaction: MAVEN solar wind ion analyzer in-flight performance and science results. *Journal of Geophysical Research: Space Physics*, *122*, 547–578. <https://doi.org/10.1002/2016ja023167>

Halekas, J., Taylor, E., Dalton, G., Johnson, G., Curtis, D., McFadden, J., et al. (2015). The solar wind ion analyzer for MAVEN. *Space Science Reviews*, *195*(1–4), 125–151. <https://doi.org/10.1007/s11214-013-0029-z>

Harada, Y., Halekas, J., Xu, S., DiBraccio, G., Ruhunusiri, S., Hara, T., et al. (2020). Ion jets within current sheets in the Martian magnetosphere. *Journal of Geophysical Research: Space Physics*, *125*, e2020JA028576. <https://doi.org/10.1029/2020ja028576>

Leblanc, F., Witasse, O., Liliensten, J., Frahm, R. A., Safaenili, A., Brain, D. A., et al. (2008). Observations of aurorae by SPICAM ultraviolet spectrograph on board Mars express: Simultaneous ASPERA-3 and MARSIS measurements. *Journal of Geophysical Research*, *113*, 8311. <https://doi.org/10.1029/2008JA013033>

Leblanc, F., Witasse, O., Winningham, J., Brain, D., Liliensten, J., Bnelly, P.-L., et al. (2006). Origins of the Martian aurora observed by spectroscopy for investigation of characteristics of the atmosphere of Mars (SPICAM) on board Mars express. *Journal of Geophysical Research*, *111*, 9313. <https://doi.org/10.1029/2006JA011763>

Liemohn, M. W., Ma, Y., Nagy, A., Kozyra, J., Winningham, J., Frahm, R., et al. (2007). Numerical modeling of the magnetic topology near Mars auroral observations. *Geophysical Research Letters*, *34*(24), L24202. <https://doi.org/10.1029/2007gl031806>

Lillis, R. J., & Brain, D. A. (2013). Nightside electron precipitation at Mars: Geographic variability and dependence on solar wind conditions. *Journal of Geophysical Research: Space Physics*, *118*, 3546–3556. <https://doi.org/10.1002/jgra.50171>

Lillis, R. J., Deighan, J., Brain, D., Fillingim, M., Jain, S., Chaffin, M. et al. (2022). First Synoptic Images of FUV Discrete Aurora and Discovery of Sinuous Aurora at Mars by EMM EMUS. *Geophysical Research Letters*. <https://doi.org/10.1029/2022GL099820>

Lillis, R. J., Mitchell, D. L., Steckiewicz, M., Brain, D., Xu, S., Weber, T., et al. (2018). Ionizing electrons on the Martian nightside: Structure and variability. *Journal of Geophysical Research: Space Physics*, *123*, 4349–4363. <https://doi.org/10.1029/2017ja025151>

Luhmann, J., Dong, C., Ma, Y., Curry, S., Xu, S., Lee, C., et al. (2017). Martian magnetic storms. *Journal of Geophysical Research: Space Physics*, *122*, 6185–6209. <https://doi.org/10.1002/2016ja023513>

Mauk, B. H., Clark, G., Gladstone, G. R., Kotsiaros, S., Adriani, A., Allegrini, F., et al. (2020). Energetic particles and acceleration regions over Jupiter's polar cap and main aurora: A broad overview. *Journal of Geophysical Research: Space Physics*, *125*, e2019JA027699. <https://doi.org/10.1029/2019ja027699>

Mauk, B. H., Haggerty, D., Paranicas, C., Clark, G., Kollmann, P., Rymer, A., et al. (2017). Discrete and broadband electron acceleration in Jupiter's powerful aurora. *Nature*, *549*(7670), 66–69. <https://doi.org/10.1038/nature23648>

- McClintock, W. E., Schneider, N. M., Holsclaw, G. M., Clarke, J. T., Hoskins, A. C., Stewart, I., et al. (2015). The imaging ultraviolet spectrograph (IUVS) for the MAVEN mission. *Space Science Reviews*, 195(1–4), 75–124. <https://doi.org/10.1007/s11214-014-0098-7>
- McFadden, J., Kortmann, O., Curtis, D., Dalton, G., Johnson, G., Abiad, R., et al. (2015). MAVEN suprathermal and thermal ion composition (STATIC) instrument. *Space Science Reviews*, 195(1–4), 199–256. <https://doi.org/10.1007/s11214-015-0175-6>
- Mitchell, D., Mazelle, C., Sauvaud, J.-A., Thocaven, J.-J., Rouzaud, J., Fedorov, A., et al. (2016). The MAVEN solar wind electron analyzer. *Space Science Reviews*, 200(1–4), 495–528. <https://doi.org/10.1007/s11214-015-0232-1>
- Morschhauser, A., Lesur, V., & Grott, M. (2014). A spherical harmonic model of the lithospheric magnetic field of Mars. *Journal of Geophysical Research: Planets*, 119, 1162–1188. <https://doi.org/10.1002/2013je004555>
- Ruhunusiri, S., Halekas, J. S., Espley, J. R., Eparvier, F., Brain, D., Mazelle, C., et al. (2018). An artificial neural network for inferring solar wind proxies at Mars. *Geophysical Research Letters*, 45(20), 10855–10865. <https://doi.org/10.1029/2018GL079282>
- Schneider, N. M., Deighan, J. I., Jain, S. K., Stiepen, A., Stewart, A. I. F., Larson, D., et al. (2015). Discovery of diffuse aurora on Mars. *Science*, 350(6261), aad0313. <https://doi.org/10.1126/science.aad0313>
- Schneider, N. M., Jain, S. K., Deighan, J., Nasr, C. R., Brain, D. A., Larson, D., et al. (2018). Global aurora on Mars during the September 2017 space weather event. *Geophysical Research Letters*, 45(15), 7391–7398. <https://doi.org/10.1029/2018gl077772>
- Schneider, N. M., Milby, Z., Jain, S. K., Gard, J.-C., Soret, L., Brain, D. A., et al. (2021). Discrete aurora on Mars: Insights into their distribution and activity from MAVEN/IUVS observations. *Journal of Geophysical Research: Space Physics*, 126, e2021JA029428. <https://doi.org/10.1029/2021JA029428>
- Soret, L., Gérard, J.-C., Libert, L., Shematovich, V. I., Bisikalo, D. V., Stiepen, A., & Bertaux, J.-L. (2016). SPICAM observations and modeling of Mars aurorae. *Icarus*, 264, 398–406. <https://doi.org/10.1016/j.icarus.2015.09.023>
- Soret, L., Gérard, J.-C., Schneider, N., Jain, S., Milby, Z., Ritter, B., et al. (2021). Discrete aurora on Mars: Spectral properties, vertical profiles, and electron energies. *Journal of Geophysical Research: Space Physics*, 126, e2021JA029495. <https://doi.org/10.1029/2021ja029495>
- Weber, T., Brain, D., Mitchell, D., Xu, S., Connerney, J., & Halekas, J. (2017). Characterization of low-altitude nightside Martian magnetic topology using electron pitch angle distributions. *Journal of Geophysical Research: Space Physics*, 122, 9777–9789. <https://doi.org/10.1002/2017JA024491>
- Weber, T., Brain, D., Mitchell, D., Xu, S., Espley, J., Halekas, J., et al. (2019). The influence of solar wind pressure on Martian crustal magnetic field topology. *Geophysical Research Letters*, 46(5), 2347–2354. <https://doi.org/10.1029/2019gl081913>
- Weber, T., Brain, D., Xu, S., Mitchell, D., Espley, J., Halekas, J., et al. (2020). The influence of interplanetary magnetic field direction on Martian crustal magnetic field topology. *Geophysical Research Letters*, 47(19), e2020GL087757. <https://doi.org/10.1029/2020gl087757>
- Withers, P. (2009). A review of observed variability in the dayside ionosphere of Mars. *Advances in Space Research*, 44(3), 277–307. <https://doi.org/10.1016/j.asr.2009.04.027>
- Xu, S., Curry, S. M., Mitchell, D. L., Luhmann, J. G., Lillis, R. J., & Dong, C. (2019). Magnetic topology response to the 2003 Halloween ICME event at Mars. *Journal of Geophysical Research: Space Physics*, 124, 151–165. <https://doi.org/10.1029/2018ja026118>
- Xu, S., Fang, X., Mitchell, D. L., Ma, Y., Luhmann, J. G., DiBraccio, G. A., et al. (2018). Investigation of Martian magnetic topology response to 2017 September ICME. *Geophysical Research Letters*, 45(15), 7337–7346. <https://doi.org/10.1029/2018gl077708>
- Xu, S., Mitchell, D. L., McFadden, J. P., Fillingim, M. O., Andersson, L., Brain, D. A., et al. (2020). Inverted-V electron acceleration events occurring with localized auroral observations at Mars by MAVEN. *Geophysical Research Letters*, 47(9), e2020GL087414. <https://doi.org/10.1029/2020gl087414>
- Xu, S., Mitchell, D. L., McFadden, J. P., Schneider, N. M., Milby, Z., Jain, S., et al. (2022). Empirically determined auroral electron events at Mars—MAVEN observations. *Geophysical Research Letters*, 49(6), e2022GL097757. <https://doi.org/10.1029/2022GL097757>
- Xu, S., Weber, T., Mitchell, D. L., Brain, D. A., Mazelle, C., DiBraccio, G. A., & Espley, J. (2019). A technique to infer magnetic topology at Mars and its application to the terminator region. *Journal of Geophysical Research: Space Physics*, 124, 1823–1842. <https://doi.org/10.1029/2018ja026366>